Editors' Suggestion | Featured in Physics

Streamwise Dissolution Patterns Created by a Flowing Water Film

Adrien Guérin, Julien Derr, Sylvain Courrech du Pont, and Michael Berhanu*
MSC, Université de Paris, Université Paris Diderot, CNRS (UMR 7057), 75013 Paris, France

(Received 7 July 2020; accepted 2 October 2020; published 6 November 2020)

The dissolution of rocks by rainfall commonly generates streamwise parallel channels, yet the occurrence of these natural patterns remains to be understood. Here, we report the emergence in the laboratory of a streamwise dissolution pattern at the surface of an initially flat soluble material, inclined and subjected to a thin runoff water flow. Nearly parallel grooves about 1 mm wide and directed along the main slope spontaneously form. Their width and depth increase continuously with time until their crests emerge and channelize the flow. Our observations may constitute the early stage of the patterns observed in the field.

DOI: 10.1103/PhysRevLett.125.194502

Pattern formation arising from mechanical erosion has been the subject of numerous physics studies [1–3]. In contrast, morphogenesis due to chemical erosion has received far less attention outside the geological community [4,5]. Yet, it is the dominant erosive process for soluble rocks such as limestone ($CaCO_3$), gypsum ($CaSO_4, 2H_2O$), and salt (NaCl). When the rock is in contact with a water flow, it dissolves into the flow and becomes a solute. The rock erosion rate then depends on the local solute concentration at the dissolving interface. This concentration can vary due to hydrodynamics, explaining the emergence of specific dissolution patterns [4,5]. In caves, solutal convection [6–10] and turbulent flows [11–14] shape dissolution pits and scallops. At the Earth's surface, when rock is exposed to rainfall, the runoff flow typically creates nearly parallel channels called *Rillenkarren* in the geomorphology literature. These channels are directed along the main slope, and their width ranges from about 1 mm to 1 m [15,16] [see Fig. 1(a), 1(b)]. Although their occurrence is common in nature, the physical origin of this streamwise pattern remains unknown.

At the surface of a granular bed, streamwise grooves can be generated by counterrotating vortices when the flow is turbulent [17,18] or by the diffusion-like transport of grains from the troughs to the crests of the bed in a laminar regime [19]. Yet, when water flows over a melting, dissolving, or precipitating bed, stability analyses only predict spanwise (or transverse) undulations due to a coupling between the free surface of the flow and the bed [20–22]. Streamwise patterns on soluble rocks have only been predicted for thin film flows overhung by the rock, which are destabilized by the gravity [23–25].

Experimentally, turbulent flows of about 0.5 m/s in a deep-water regime have been found to generate streamwise grooves called flutes on plates of plaster [26] (same chemical composition as gypsum). This streamwise dissolution pattern can evolve into a transverse pattern commonly called scallops, but Allen [26] did not monitor the pattern change and proposed only qualitative mechanisms. Finally, a single study reports the formation of streamwise grooves in experimental conditions close to the *Rillenkarren* ones [27,28]. Molded blocks of plaster and salt blocks were subjected to an artificial rain generating a

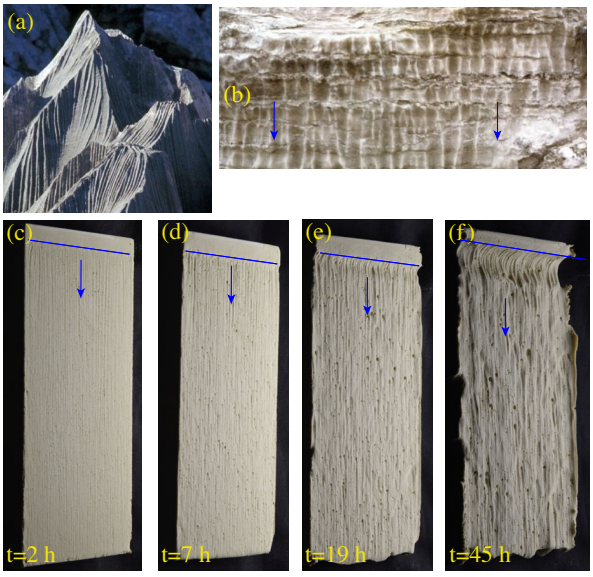

FIG. 1. (a) Natural *Rillenkarren* on limestone (Karst plateau, Slovenia). Credit: Marko Simic. Width of picture: about 1 m. (b) Dissolution rills or *Rillenkarren* on gypsum (Vaucluse, France). Width of picture: about 20 cm. Credit: Pierre Thomas (https://planet-terre.ens-lyon.fr). (c)–(f) Experimental dissolution grooves. Consecutive pictures of a gypsum (plaster of Paris) block subjected to a runoff flow (inclination 39°, flow rate $Q = 2.8$ L/ min, $U = 0.84$ m/s) for increasing times of exposure to the flow. From left to right, $t = 2$, 7, 19, and 45 h. The blue lines indicate the position of water injection and the blue arrows the flow direction (b)–(f). The initial dimensions of the block are $200 \times 100 \times 25$ mm.

flow of a few centimeters per second and around 100 μm deep. After several hundred hours, grooves several centimeters wide were obtained. This descriptive study does not investigate the initiation or the temporal evolution of this pattern. Moreover, several authors claim that the impact of the rain droplets on the water film is the condition that generates the grooves [16,28,29].

Here, we demonstrate experimentally the emergence of streamwise dissolution patterns created by a water film flowing on soluble rocks in the absence of rainfall. Figure 1(c)–1(f) shows the results of an experiment performed on a block of plaster of Paris (KRONE Alabaster Modellgips 80, pure gypsum; see Supplemental Material [30], which includes Refs. [31–38]). Millimeter-wide grooves directed along the main slope appear after several dozens of minutes. Over time, the characteristic width and depth of the grooves increase until they are so deep that their crests emerge from the water film, thus channelizing the flow. At this stage, these centimetric grooves are similar to the *Rillenkarren* observed in the field.

Experiments with limestone are difficult to perform in reasonable time as limestone dissolves slowly. We also performed experiments on carved blocks of Himalayan pink salt (Khewra Salt Mine, Pakistan, 98% sodium chloride [39]). Although these blocks are natural geological samples and present a significant heterogeneity in structure, with chemical defects and cracks, we observed qualitatively similar streamwise grooves (see Supplemental Material [30]).

Figure 2(a) depicts the principle of the experiment. A constant flow rate Q of tap water is injected on top of molded rectangular blocks of plaster ($200\times 100\times 25$ mm). Thanks to the excellent wetting properties of soluble materials, a thin water film of homogeneous thickness h spans all the block after a transient of a few seconds. Driven by gravity, the film flows over the top surface of the block inclined with an angle θ. We measure the average film thickness h with the flight time of an ultrasonic beam and then deduce the average velocity U (Supplemental Material [30]), for the initial flat bed. For example, with a typical flow rate $Q = 2.8$ L/ min and an inclination $\theta = 39°$, we measure a thickness $h = 560$ μm and calculate a velocity $U \approx 0.84$ m/s. The corresponding Reynolds and Froude numbers are $\mathrm{Re} = (Uh)/\nu \approx 466$ and $Fr = U/\sqrt{gh} \approx 11$ (with $g = 9.81$ m s^{-2} the gravitational acceleration and ν the kinematic viscosity of fresh water $\nu = 1.0\times 10^{-6}$ m^2 s^{-1} at 20 °C). According to experimental [40] and numerical works [41], these thin flowing films belong to a regime of wall-induced turbulence ($\mathrm{Re} > 75$).

Measuring the topography of a rock while a thin film of water flows over it is a difficult task. Instead, we regularly stop the experiment and measure the three-dimensional topography of the dried eroded surface using a laser scanner. We thus obtain the surface elevation $\eta(x, y, t)$

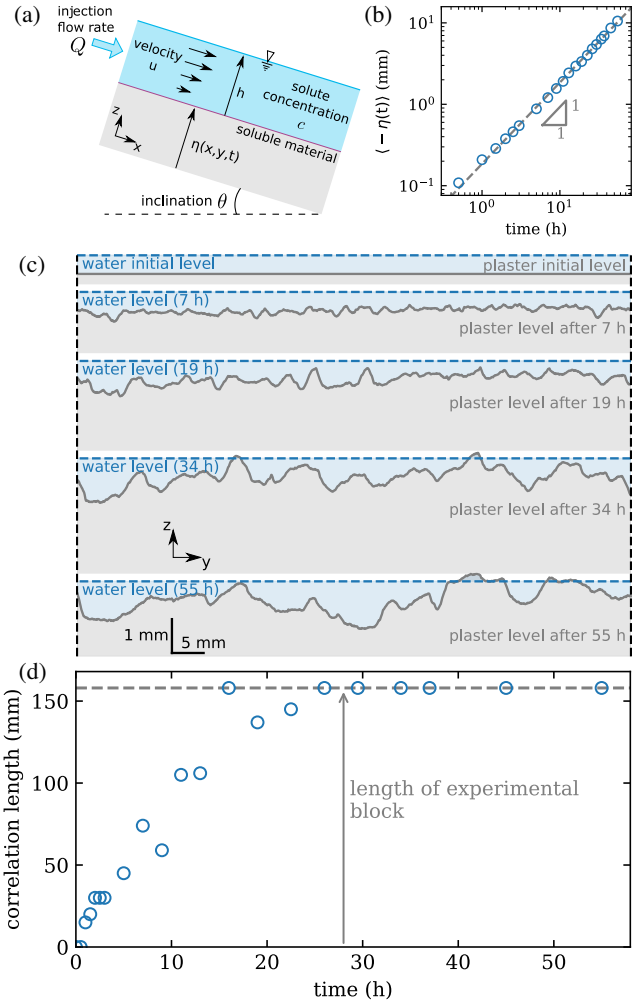

FIG. 2. (a) Sketch of the dissolution experiment, side view. A water film of flow rate Q, velocity U, and thickness h is driven by gravity and flows over a block of soluble rock of width $W = 100$ mm, length $L = 200$ mm, and inclined at an angle θ. The block thickness $\eta(x, y, t)$ progressively decreases as it dissolves, creating a solute concentration field $c(x, y, z)$ in the flow. (b) As a result, the surface-averaged dissolved depth $\langle -\eta \rangle$ increases linearly (here during a typical experiment with $U = 0.84$ m/s, $h = 380$ μm). (c) Transverse profiles $\eta(x, y, t)$ of the same experiment, measured along y at a distance $x = 20$ mm from the water injection and plotted at various times t. The water level is deduced by flow conservation. Thin grooves grow over an initially flat surface and finally form channels, their crests emerging from the flow. (d) As the streamwise pattern grows, the longitudinal correlation length, which measures the maximum distance along x between two correlated transverse profiles, increases until it reaches the length of the block.

with an accuracy of 70 μm and a resolution in (x, y) of 0.2 mm at several time steps ranging from 0.5 to 10 h. We can then analyze the topography evolution of the plaster blocks. As an example, let us describe a typical 55 h-long experiment with $U = 0.84$ m/s and $h = 560$ μm. As water dissolves the gypsum and flows downward, the solute concentration increases. The erosion resulting from this

dissolution is thus slower far from the injection, as the solute concentration gets closer to its saturation value. The erosion dynamics and the resulting shaping of longitudinal profiles will be studied in a further work, and we only stress here that the surface-averaged erosion $\langle -\eta(t)\rangle$ of the rock is linear in time, which means that the erosion rate of the block is constant [Fig. 2(b)].

After 30 minutes of exposure to the flow, streamwise thin grooves become visible. In Fig. 2(c), consecutive transverse profiles $\eta(x, y, t)$ represent the progressive erosion of the rock at a distance $x = 20$ mm from the water injection. The associated water height deduced by flow conservation is also displayed. As time grows, the grooves' amplitude and width increase. The thin grooves progressively merge into the large ones, which eventually channelize the flow.

At the beginning, the grooves are a few centimeters long and randomly distributed over the rock surface. Then, they progressively extend all along the block. We measure the streamwise coherence of the pattern by measuring the cross-correlation coefficient between transverse profiles. As the distance d separating the profiles along the x axis grows, the correlation coefficient decreases. We define the correlation length as the distance d where the correlation coefficient becomes smaller than a threshold, chosen to be 0.2 (see Supplemental Material [30]). Figure 2(d) shows that the correlation length increases with time and eventually reaches, after about 25 h, a saturation value corresponding to the sample size. Then, the grooves span the whole length of the block.

We measure the typical wavelength of a profile by computing the weighted average of its Fourier spectrum (see Supplemental Material [30]). As it is constant over the length of the block, we estimate the grooves' typical width λ_m as the average profile's wavelength. Figure 3(a) shows that it grows during the whole experiment from about 0.6 to 10 mm in 55 h. The pattern amplitude, estimated by the profile standard deviation σ_η minus the initial rugosity and averaged over the length of the block, also increases, almost linearly, during the whole experiment [Fig. 3(b)].

We now analyze five experiments performed on plaster with velocities varying from 0.36 to 0.84 m/s and three block inclinations of 25, 39, and 66° (see Supplemental Material [30]). Figure 3(c),(d) shows the grooves' width and amplitude, respectively, divided by the eroded depth $\langle -\eta(t)\rangle$. With this rescaling, the data belonging to different runs are gathered.

Finally, the grooves' aspect ratio seems to be controlled by the water depth. Indeed, Fig. 3(e) represents λ_m as a function of σ_η, both rescaled by the water depth h, which is the natural length scale of the problem. The different points obtained at different times and several velocities all collapse on to the same curve. The initial value of λ_m/h varies from 0.8 to 1.5, showing that the first pattern wavelength is of order of the water depth. Then, as long as $\sigma_\eta/h \lesssim 1$, λ_m and σ_η evolve proportionally, with

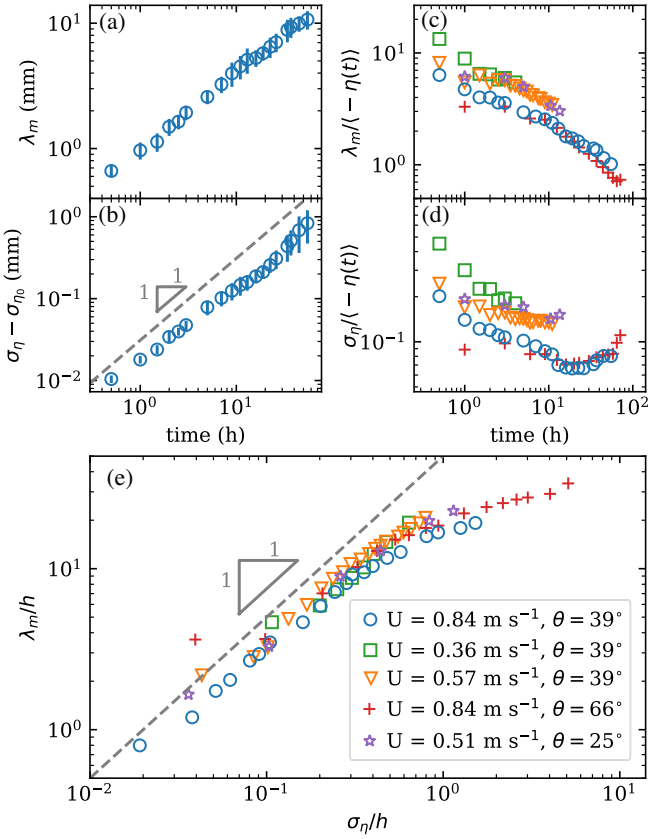

FIG. 3. Evolution of grooves' morphology during five experiments. Blue circle: $Q = 2.8$ L/min, $\theta = 39°$, $U = 0.84$ m/s, and $h = 556$ μm. Green square: $Q = 0.22$ L/min, $\theta = 39°$, $U = 0.36$ m/s, and $h = 101$ μm. Orange down-pointing triangle: $Q = 0.86$ L/min, $\theta = 39°$, $U = 0.57$ m/s, and $h = 255$ μm. Red plus: $Q = 1.9$ L/min, $\theta = 66°$, $U = 0.84$ m/s, and $h = 380$ μm. Magenta star: $Q = 0.93$ L/min, $\theta = 25°$, $U = 0.51$ m/s, and $h = 305$ μm. (a) The groove typical wavelength λ_m increases with time. (b) The pattern amplitude $\sigma_\eta(t) - \sigma_\eta(t = 0)$ grows linearly with time. The error bars display the standard deviation along the x axis. (c) Grooves' typical wavelength rescaled by the dissolved depth $\lambda_m/|\langle\eta\rangle|$ versus time. (d) Pattern amplitude rescaled by the dissolved depth $\sigma_\eta/|\langle\eta\rangle|$ versus time. (e) Grooves' wavelengths with respect to their amplitude, both rescaled by the water depth. The aspect ratio seems to be controlled by the flow depth.

$\lambda_m \approx 20\ \sigma_\eta$. When the pattern amplitude exceeds the water height, i.e., $\sigma_\eta \gtrsim h$, λ evolves more slowly than σ_η, meaning that the grooves' aspect ratio is no longer conserved. In this channelization regime, the channel crests start to emerge from the water film. The flow thus keeps on dissolving the troughs while the crests are more preserved such that the channels' depth increases faster than their width.

In this experimental study, we demonstrate that streamwise dissolution patterns are created by a water runoff flow of constant thickness. This observation contradicts the affirmation that the impact of rain drops is required to create the dissolution rills observed in the field [28]. To our

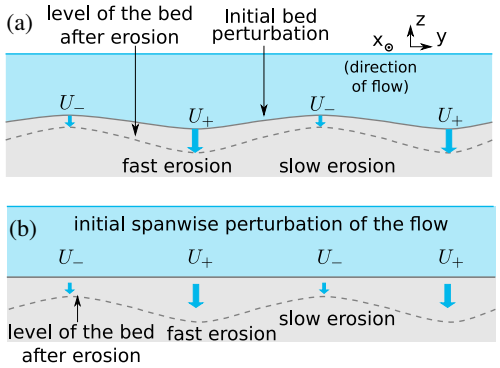

FIG. 4. Two scenarios of appearance of a streamwise dissolution pattern. (a) An initial perturbation of the bed is amplified because the local velocity increases with the fluid depth for a gravity driven flow. (b) The flow contains a transverse velocity variation, which is imprinted on the bed.

knowledge, such streamwise dissolution patterns have not yet been predicted theoretically.

Dissolution patterns result from a spatial heterogeneity of the erosion rate, which can be caused by local variations of the flow velocity. Indeed, a larger velocity decreases the thickness of the solute concentration boundary layer at the dissolving interface, which increases the local erosion rate. Thus, we propose two kinds of mechanisms to explain the pattern emergence.

First, grooves could stem from a feedback mechanism between the topography and the flow, leading to a destabilization of the bed. For a gravity-driven flow, the local velocity increases with the water depth. Thus, any initial perturbation of the bed would be amplified, as displayed in Fig. 4(a). A simple linear stability analysis in the spanwise plane indeed predicts that all wavelengths are unstable and an exponential growth (Supplemental Material [30]). However, experimentally the pattern grows linearly at short times. Moreover, the initial grooves' width could be imposed by the defects of the dissolving surface like small-scale roughness or chemical heterogeneities. Yet, the grooves' morphology is similar in salt and plaster experiments (see pictures in Supplemental Material [30]) and on gypsum and limestone [Fig. 1(a), 1(b)]. The regularity of their morphology on various materials suggests that this pattern does not depend on the material heterogeneities, which vary from one material to the other, but rather on a purely hydrodynamic mechanism.

Patterns could also arise because of the hydrodynamics only, being an imprint of heterogeneities in the flow. If the velocity profile presents transverse variations, as shown in Fig. 4(b), the pattern would then appear as a passive response of the dissolving bed to the flow, which would impose the initial wavelength λ_m. A similar scenario has been proposed for the emergence of dissolution patterns in solutal convection [9,42]. Here, by taking, for example, $U = U_0[1 + \beta\cos(ky)]$ and modeling simply the solute advection, we predict that the pattern evolution velocity $d\sigma_\eta/dt$ is proportional to the global erosion velocity $d|\langle\eta(t)\rangle|/dt$ by a factor $\beta/2$ (Supplemental Material [30]). Although justified only at short times, this model implies a linear growth of the pattern amplitude and a constant value of the ratio $\sigma_\eta/|\langle\eta\rangle|$, which are both observed in our experiments [Fig. 3(b),3(d)]. However, we do not know of such hydrodynamic structures reported in the literature, such that β and k are unknown. They must have a sufficient lifetime to have a significant influence, as the erosion velocity is several orders of magnitude smaller than the flow velocity. For a turbulent, deep-water flow, Allen explains qualitatively the appearance of grooves and furrows on plaster blocks by the presence of turbulent coherent structures [26], like the turbulent streaks [43,44] inside the viscous sublayer or the Görtler vortices [45] due to the substrate curvature. After initiation, the structure locations could be locked at the positions of the first ridges, which could fix the phase of the pattern during its evolution. A decisive proof of the existence of these structures in the conditions of our experiment is difficult to obtain, as hydrodynamic measurements in films thinner than 1 mm are challenging. In the conditions of our experiments, the flow belongs to a wall-induced turbulence regime [40,41], and the presence of turbulent structures cannot be excluded. Yet, the wavelengths of these structures are predicted theoretically only in semi-infinite domains. Moreover, such structures have never been reported in shallow flows, and we must note the absence of any experimental or numerical velocity field characterization of turbulent falling films [41]. Our experimental results suggest that such structures may exist, and thus we stress that the hydrodynamics of falling films at large Reynolds numbers still present unknown features that could strongly affect mass and heat fluxes. The film thickness h is a natural length scale and seems to control the morphology of the grooves observed in our experiment. The emergence and shape of flow structures into a thin flowing film probably requires one to take full account of this length scale.

In the field, the *Rillenkarren* are created by a rainfall-generated flow, which presents significantly smaller depth and velocity than our experiments [28]. However, the impacts of millimetric drops could efficiently induce small-scale turbulence [46] and generate spanwise perturbations to the velocity field. Once they have emerged at the earliest stages of the experiment, the grooves then grow continuously in length, width, and depth. This suggests that the *Rillenkarren* observed in the field are probably a snapshot of a continuous evolution. If this is the case, the *Rillenkarren* dimensions would indicate their age, that is, their time of exposure to rainfall.

Finally, the long-term evolution of the pattern deserves further study. Our results show that once the grooves' depth becomes comparable to the flow depth, their crests emerge

from the flow and the grooves channelize the flow. Then, they enter a new growth regime where their width grows much more slowly than their depth. Understanding this growth regime would need to take into account the feedback of the evolving topography on the flow. In deep-water flows, the dissolution patterns tend to evolve into traverse patterns called scallops [9,26]. Here, the flow channelization may prevent the development of such transverse instabilities.

We thank Valentin Leroy for his help with the ultrasonic measurements, Alexandre Di Palma for technical assistance, and Jean-Gabriel Pichon for experimental work with salt blocks. We acknowledge Piotr Szymczak, Matteo Bertagni, and Carlo Camporeale for discussions. This research was funded by the ANR grant Erodiss ANR-16-CE30-0005.

*Corresponding author.
michael.berhanu@univ-paris-diderot.fr

[1] F. Charru, B. Andreotti, and P. Claudin, Sand ripples and dunes, Annu. Rev. Fluid Mech. **45**, 469 (2013).
[2] S. Courrech du Pont, Dune morphodynamics, C.R. Phys. **16**, 118 (2015).
[3] D. J. Jerolmack and K. E. Daniels, Viewing Earth's surface as a soft matter landscape, Nat. Rev. Phys. **1**, 716 (2019).
[4] P. Meakin and B. Jamtveit, Geological pattern formation by growth and dissolution in aqueous systems, Proc. R. Soc. A **466**, 659 (2010).
[5] B. Jamtveit and O. Hammer, Sculpting of rocks by reactive fluids, Geochem. Perspect. **1**, 341 (2012), https://pubs.geoscienceworld.org/perspectives/article-abstract/1/3/341/138767/.
[6] T. S. Sullivan, Y. Liu, and R. E. Ecke, Turbulent solutal convection and surface patterning in solid dissolution, Phys. Rev. E **54**, 486 (1996).
[7] C. Cohen, M. Berhanu, J. Derr, and S. Courrech du Pont, Erosion patterns on dissolving and melting bodies (2015 Gallery of fluid motion), Phys. Rev. Fluids **1**, 050508 (2016).
[8] M. S. Davies Wykes, J. M. Huang, G. A. Hajjar, and L. Ristroph, Self-sculpting of a dissolvable body due to gravitational convection, Phys. Rev. Fluids **3**, 043801 (2018).
[9] C. Cohen, M. Berhanu, J. Derr, and S. Courrech du Pont, Buoyancy driven dissolution of inclined blocks: Erosion rate and pattern formation, Phys. Rev. Fluids **5**, 053802 (2020).
[10] S. Pegler and M. S. Davies Wykes, Shaping of melting and dissolving solids under natural convection, J. Fluid Mech. **900**, A35 (2020).
[11] J. Huang, M. Moore, and L. Ristroph, Shape dynamics and scaling laws for a body dissolving in fluid flow, J. Fluid Mech. **765**, R3 (2015).
[12] M. Moore, Riemann-Hilbert problems for the shapes formed by bodies dissolving, melting, and eroding in fluid flows, Commun. Pure Appl. Math. **70**, 1810 (2017).
[13] P. Blumberg and R. Curl, Experimental and theoretical studies of dissolution roughness, J. Fluid Mech. **65**, 735 (1974).
[14] P. Claudin, O. Durán, and B. Andreotti, Dissolution instability and roughening transition, J. Fluid Mech. **832**, R2 (2017).
[15] *Karst Rock Features, Karren Sculpturing*, edited by A. Ginés, M. Knez, T. Slabe, and W. Dreybrodt (Karst Research Institute, Zalozba ZRC, Ljubljana, 2009).
[16] J. Lundberg, Microsculpturing of solutional rocky landforms, in *Treatise on Geomorphology* (Academic Press, San Diego, 2013), Vol. 6.12 pp. 121–138.
[17] M. Colombini, Turbulence-driven secondary flows and formation of sand ridges, J. Fluid Mech. **254**, 701 (1993).
[18] M. Colombini and G. Parker, Longitudinal streaks, J. Fluid Mech. **304**, 161 (1995).
[19] A. Abramian, O. Devauchelle, and E. Lajeunesse, Streamwise streaks induced by bedload diffusion, J. Fluid Mech. **863**, 601 (2019).
[20] C. Camporeale and L. Ridolfi, Hydrodynamic-Driven Stability Analysis of Morphological Patterns on Stalactites and Implications for Cave Paleoflow Reconstructions, Phys. Rev. Lett. **108**, 238501 (2012).
[21] R. Vesipa, C. Camporeale, and L. Ridolfi, Thin-film induced morphological instabilities over calcite surfaces, Proc. R. Soc. A **471**, 20150031 (2015).
[22] M. Yokokawa, N. Izumi, K. Naito, G. Parker, T. Yamada, and R. Grevet, Cyclic steps on ice, J. Geophys. Res. Earth Surf. **121**, 1023 (2016).
[23] C. Camporeale, Hydrodynamically locked morphogenesis in karst and ice flutings, J. Fluid Mech. **778**, 89 (2015).
[24] M. B. Bertagni and C. Camporeale, Nonlinear and subharmonic stability analysis in film-driven morphological patterns, Phys. Rev. E **96**, 053115 (2017).
[25] G. Balestra, Pattern formation in thin liquid films: from coating-flow instabilities to microfluidic droplets, Ph.D. Thesis, EPFL, 2018.
[26] J. R. L. Allen, Bed forms due to mass transfer in turbulent flows: a kaleidoscope of phenomena, J. Fluid Mech. **49**, 49 (1971).
[27] J. R. Glew, The simulation of Rillenkarren, Master's thesis, McMaster University. 1977.
[28] J. R. Glew and D. C. Ford, A simulation study of the development of Rillenkarren, Earth Surface Processes **5**, 25 (1980).
[29] J. Lundberg and A. Ginés, *Karst Rock Features, Karren Sculpturing* (Karst Research Institute, Zalozba ZRC, Ljubljana, 2009). Chap. Rillenkarren, pp. 185–210.
[30] See Supplemental Material at http://link.aps.org/supplemental/10.1103/PhysRevLett.125.194502 for description of the experimental device, flow characterization, data processing methods, and additional experimental pictures. We provide also two simplified models in order to explain the pattern emergence.
[31] S. Kalliadasis, C. Ruyer-Quil, B. Scheid, and M. Velarde, *Falling Liquid Films* (Springer-Verlag, London, 2012).
[32] F. Charru, *Hydrodynamic Instabilities* (Cambridge University Press, Cambridge, England, 2011).

[33] W. Thielicke and E. Stamhuis, Pivlab towards user-friendly, affordable and accurate digital particle image velocimetry in matlab, J. Open Res. Software **2**, e30 (2014).
[34] J. Liu, J. D. Paul, and J. P. Gollub, Measurements of the primary instabilities of film flows, J. Fluid Mech. **250**, 69 (1993).
[35] J. Colombani and J. Bert, Holographic interferometry study of the dissolution and diffusion of gypsum in water, Geochim. Cosmochim. Acta **71**, 1913 (2007).
[36] *The Handbook of Chemistry and Physics*, edited by D. R. Lide (CRC Press, Boca Raton, FL, 2004).
[37] M. Alkattan, E. H. Oelkers, J.-L. Dandurand, and J. Schott, Experimental studies of halite dissolution kinetics, 1 the effect of saturation state and the presence of trace metals, Chem. Geol. **137**, 201 (1997).
[38] J. Crank, *The Mathematics of Diffusion* (Clarendon Press, Oxford, 1975).
[39] Q. M. Sharif, M. Hussain, and M. T. Hussain, Chemical evaluation of a major salt deposits of Pakistan, Journal of the Chemical Society of Pakistan **29**, 569 (2007), https://jcsp.org.pk/issueDetail.aspx?aid=1317228d-9385-4680-bb35-aa5e6e093278.
[40] S. Ishigai, S. Nakanisi, T. Koizumi, and Z. Oyabu, Hydrodynamics and heat transfer of vertically falling liquid films, Bull. JSME **15**, 594 (1972).
[41] G. F. Dietze, W. Rohlfs, K. Nährich, R. Kneer, and B. Scheid, Three-dimensional flow structures in laminar falling liquid films, J. Fluid Mech. **743**, 75 (2014).
[42] J. Philippi, M. Berhanu, J. Derr, and S. Courrech du Pont, Solutal convection induced by dissolution, Phys. Rev. Fluids **4**, 103801 (2019).
[43] S. J. Kline, W. C. Reynolds, F. A. Schraub, and P. Runstadler, The structure of turbulent boundary layers, J. Fluid Mech. **30**, 741 (1967).
[44] S. I. Chernyshenko and M. F. Baig, The mechanism of streak formation in near-wall turbulence, J. Fluid Mech. **544**, 99 (2005).
[45] W. S. Saric, Görtler vortices, Annu. Rev. Fluid Mech. **26**, 379 (1994).
[46] E. L. Harrison and F. Veron, Near-surface turbulence and buoyancy induced by heavy rainfall, J. Fluid Mech. **830**, 602 (2017).